Atomistic Simulation of Realistically Sized Nanodevices Using NEMO 3-D—Part II: Applications

Gerhard Klimeck, *Senior Member, IEEE*, Shaikh Shahid Ahmed, Neerav Kharche, Marek Korkusinski, Muhammad Usman, Marta Prada, and Timothy B. Boykin, *Senior Member, IEEE*

(Invited Paper)

Abstract—In Part I, the development and deployment of a general nanoelectronic modeling tool (NEMO 3-D) has been discussed. Based on the atomistic valence-force field and the $sp^3d^5s^*$ nearest neighbor tight-binding models, NEMO 3-D enables the computation of strain and electronic structure in nanostructures consisting of more than 64 and 52 million atoms, corresponding to volumes of $(110 \text{ nm})^3$ and $(101 \text{ nm})^3$, respectively. In this part, successful applications of NEMO 3-D are demonstrated in the atomistic calculation of single-particle electronic states of the following realistically sized nanostructures: 1) self-assembled quantum dots (QDs) including long-range strain and piezoelectricity; 2) stacked quantum dot system as used in quantum cascade lasers; 3) SiGe quantum wells (QWs) for quantum computation; and 4) SiGe nanowires. These examples demonstrate the broad NEMO 3-D capabilities and indicate the necessity of multimillion atomistic electronic structure modeling.

Index Terms—Atomistic simulation, Keating model, nanostructures, nanowire, NEMO 3-D, piezoelectricity, quantum computation, quantum dot (QD), quantum well (QW), strain, tight binding, valley splitting (VS).

I. INTRODUCTION

THIS paper describes NEMO 3-D capabilities in the simulation of three different classes of nanodevices of carrier confinement in three, two, and one dimension in the GaAs/InAs and SiGe materials systems.

Single and Stacked Quantum Dots (QDs, Confinement in Three Dimensions): QDs are solid-state semiconducting nanostructures that provide confinement of charge carriers (electrons, holes, and excitons) in all three spatial dimensions, resulting in strongly localized wave functions, discrete energy eigenvalues, and subsequent interesting physical and novel device properties [1]–[5]. Existing nanofabrication techniques tailor QDs in a variety of types, shapes, and sizes. Within bottom–up approaches, QDs can be realized by colloidal synthesis at benchtop conditions. QDs thus created have dimensions ranging from 2 to 10 nm, corresponding to a range of 100–100 000 atoms. Self-assembled QDs (SAQDs), in the coherent Stranski–Krastanov heteroepitaxial growth mode, nucleate spontaneously within a lattice mismatched material system (for example, InAs grown on GaAs substrate) under the influence of strain in certain physical conditions during molecular beam epitaxy and metal–organic vapor phase epitaxy [1], [6]. The strain produces coherently strained quantum-sized islands on top of a 2-D wetting-layer. The islands can be subsequently buried to form the QD. Semiconducting QDs grown by self-assembly are of particular importance in quantum optics [7], [8] since they can be used as detectors of infrared radiation, optical memories, and in laser applications. The delta-function-like energy dependence of the density of states and the strong overlap of spatially confined electron and hole wavefunctions provide ultralow threshold current densities, high temperature stability of the threshold current, and high material and differential quantum gain/yield. Strong oscillator strength and nonlinearity in the optical properties have also been observed [1], [8]. SAQDs also have the potential for applications in quantum cryptography as single-photon sources and quantum computation [9], [10]. In electronic applications, QDs have been used to operate like a single-electron transistor and demonstrate pronounced Coulomb blockade effect. SAQDs, with an average height in the range of 1–5 nm, are typically of size (base length/diameter) ranging from 5 to 50 nm and consist of atoms ranging from 5000 to 2 000 000. Arrays of quantum mechanically coupled (stacked) SAQDs can be used as optically active regions in high-efficiency room-temperature lasers. Typical QD stacks consist of QDs ranging from 3 to 7 with a typical lateral extension in the range of 10–50 nm and
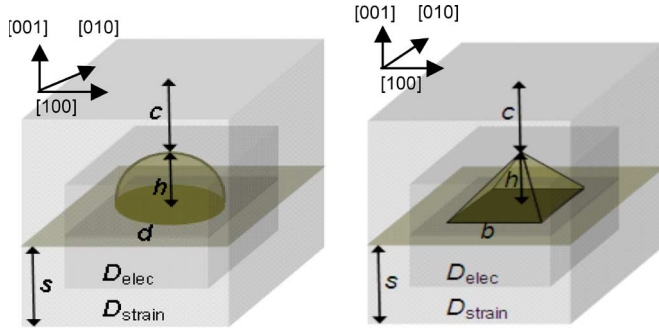
Fig. 1. Simulated InAs/GaAs QDs with dome and pyramidal shapes. Two simulation domains are shown (D_{elec}: central domain for electronic structure calculation, D_{strain}: larger/outer domain for strain calculation, s: substrate height, c: cap layer thickness, h: dot height, d: diameter, b: base length).

dot height in the range of 1–3 nm. Such dots contain atoms in the range of 5–50 million, where atomistic details of interfaces are indeed important [11].

Quantum Wires (Confinement in Two Dimensions): For quite some time, nanowires have been considered to be a promising candidate for future building blocks in computers and information processing machines [12]–[16]. Nanowires are fabricated from different materials (metal, semiconductor, insulator, and molecular) and assume different cross-sectional shapes, dimensions, and diameters. Electrical conductivity of nanowires is greatly influenced by edge effects on the surface of the nanowire and is determined by quantum mechanical conductance quanta. In the nanometer regime, the impact of surface roughness or alloy disorder on electronic band structure needs to be atomistically studied to further gauge the transport properties of nanowires.

Quantum Wells (QWs, Confinement in One Dimension): QW devices are already a de-facto standard technology in metal–oxide–semiconductor devices and QW lasers. They continue to be examined carefully for ultrascaled devices where interfacial details turn out to be critical. Composite channel materials with GaAs, InAs, InSb, GaSb, and Si are being considered [17], [18], which effectively constitute QWs. Si QWs that are buffered/strained by SiGe are considered for quantum computing (QC) devices where valley splitting (VS) is an important issue [19]. Si is desirable for QC due to its long spin-decoherence times, scaling potential, and integrability within the present microelectronic infrastructure. In strained Si, the sixfold valley degeneracy of Si is broken into lower twofold and raised fourfold valley degeneracies. The presence of twofold valley degeneracy is a potential source of decoherence, which leads to the leakage of quantum information outside qubit Hilbert space. Therefore, it is of great interest to study the lifting of the remaining twofold valley degeneracy in strained Si due to sharp confinement potentials in recently proposed [19] SiGe/Si/SiGe QW heterostructures based QC architectures.

II. SIMULATION RESULTS

A. Strain and Piezoelectricity in InAs/GaAs Single QDs

The dome- and pyramid-shaped InAs QDs that are studied first in this paper are embedded in a GaAs barrier material (schematic shown in Fig. 1), have a diameter (base length) and
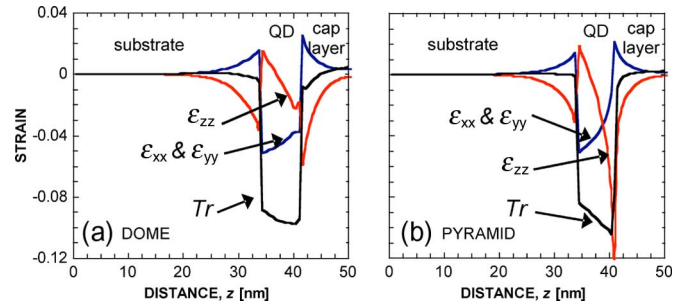

Fig. 2. Atomistic *diagonal* strain profile along the [001] z-direction. (a) Dome-shaped dot with diameter $d = 11.3$ nm and height $h = 5.65$ nm. (b) Pyramidal dot with base $b = 11.3$ nm and height $h = 5.65$ nm. Strain is seen to penetrate deep inside the substrate and the cap layer. In addition, noticeable is the gradient in the trace of the hydrostatic strain curve Tr inside the dot region that results in optical polarization anisotropy and nondegeneracy in the electronic conduction band. Atomistic strain thus lowers the symmetry of the QD. The number of atoms used in these simulations was about 5 million.

height of 11.3 and 5.65 nm, respectively, and are positioned on a 0.6-nm-thick wetting layer [20], [21]. The simulation of strain is carried out in the larger computational box (width D_{strain} and height H), while the electronic structure computation is usually restricted to the smaller domain (width D_{elec} and height H_{elec}). All the strain simulations in this category fix the atom positions on the bottom plane to the GaAs lattice constant, assuming periodic boundary conditions in the lateral dimensions and open boundary conditions on the top surface. The inner electronic box assumes closed boundary conditions with passivated dangling bonds [22]. The strain domain contains ~3 million atoms, while the electronic structure domain contains ~0.3 million atoms.

Impact of Strain: Strain modifies the effective confinement volume in the device, distorts the atom bonds in length and angles, and hence modulates the local band structure and the confined states. Fig. 2 shows the diagonal (biaxial) components of strain distribution along the [001] direction in both the QDs (cut through the center of the dot). There are two salient features in both these plots: 1) The atomistic strain is long ranged and penetrates deep into both the substrate and the cap layers, and 2) all the components of biaxial stress has a nonzero slope inside the QD region. The presence of the gradient in the trace of the hydrostatic strain introduces unequal stress in the zincblende lattice structure along the depth, breaks the equivalence of the [110] and [1$\underline{1}$0] directions, and finally breaks the degeneracy of the first excited electronic state (the so-called P level). Fig. 3 shows the wavefunction distribution for the first eight conduction band electronic states within the device region for both the dots (in a 2-D projection). Note the optical anisotropy and nondegeneracy in the first excited (P) energy level. The first P state is oriented along the [110] direction, and the second P state is oriented along the [1$\underline{1}$0] direction. The individual energy spectrum is also depicted in this figure, which reveals the value of the P-level splitting/nondegeneracy (defined as $E_{110} - E_{1\underline{1}0}$) to be about 5.73 and 10.85 meV for the dome-shaped and pyramidal QDs, respectively. Although both the two dots have the same qualitative trend in diagonal strain profiles and similar wavefunction distributions, the reason for a larger split and hence pronounced anisotropy of the P level in the pyramidal QD are due to the presence of a larger gradient
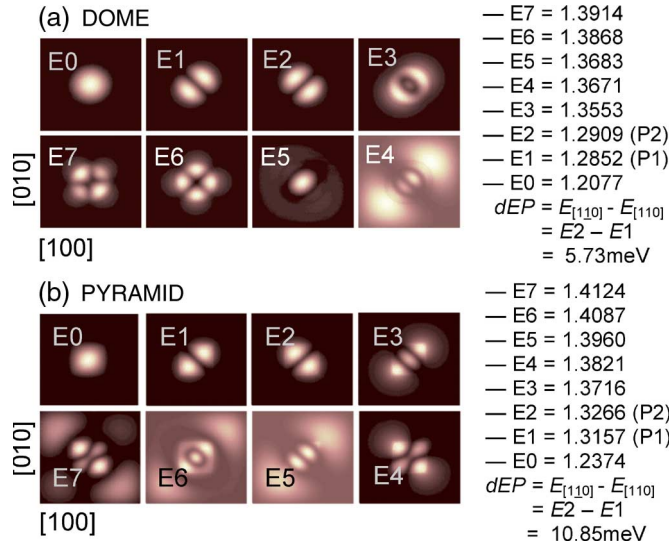
Fig. 3. Conduction band wavefunctions and spectra (in electronvolts) for the first eight energy levels in the (a) dome-shaped and (b) pyramidal QD structures. Atomistic strain is included in the calculation. Note the optical anisotropy and nondegeneracy in the P energy level. The first state is oriented along the [110] direction, and the second state is oriented along the [1$\bar{1}$0] direction.
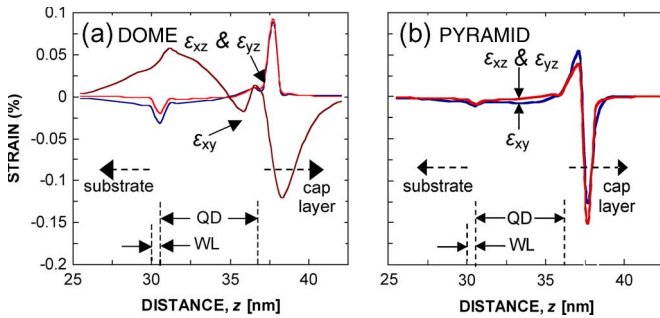

Fig. 4. Atomistic *off-diagonal* strain profile along the z (vertical) direction, which in effect induces polarization in the QD structure. (a) Dome-shaped dot with diameter $d = 11.3$ nm and height $h = 5.65$ nm. (b) Pyramidal dot with base $b = 11.3$ nm and height $h = 5.65$ nm.

Fig. 5. Potential surface plot of (a) dome-shaped and (b) pyramidal QDs in the XY plane at $z = 1$ nm from the base of the dot.

of the hydrostatic strain, as shown in Fig. 2, inside the dot region. In other words, as far as crystal symmetry lowering is concerned, atomistic strain has stronger impact in the pyramidal dot than it has in the dome-shaped dot.

Impact of Piezoelectric Field: The presence of nonzero off-diagonal strain tensor elements leads to the generation of a piezoelectric field in the QD structure, which is incorporated in the simulations as an external potential by solving the Poisson equation on the zincblende lattice. Fig. 4 shows the atomistic off-diagonal strain profiles in both the QDs with height h of 5.65 nm and a diameter (base length) of 11.3 nm. The off-diagonal strain tensors are found to be larger in the dome-shaped dot. The off-diagonal strain tensors are used to calculate the first-order polarization in the underlying crystal (please see [20] for the governing equations), which gives rise to a piezoelectric charge distribution throughout the device region and is then used to calculate the potential by solving the Poisson equation. The relevant parameters for the piezoelectric calculation are taken from [20]. Experimentally measured polarization constants of GaAs and InAs materials (on unstrained bulk)
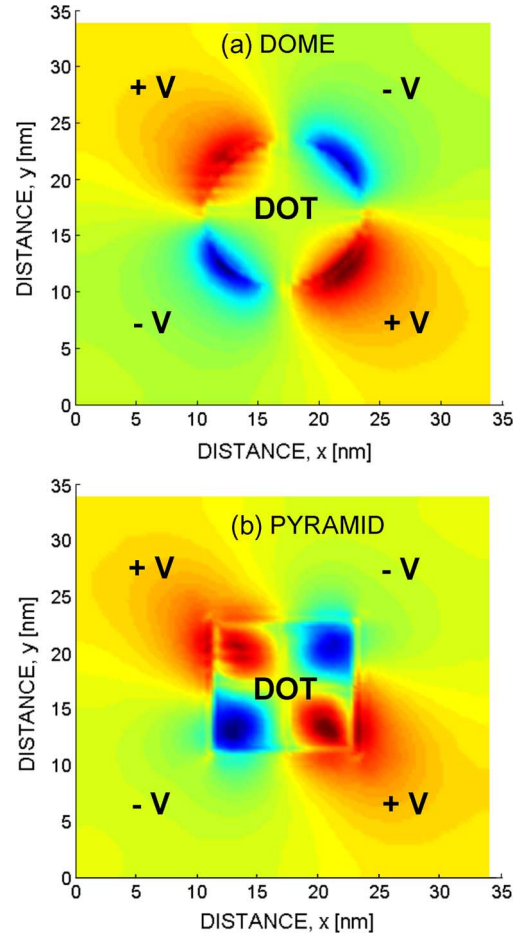
having values of -0.16 and -0.045 C/m^2 are used. The second-order piezoelectric effect [23] is neglected here because of the unavailability of reliable relevant polarization constants for an InAs/GaAs QD structures.

The calculated piezoelectric potential contour plots in the XY plane are shown in Fig. 5, revealing a pronounced polarization effect that is induced in the structure. It is found that, in both the dots, the piezoelectric field alone favors the [1$\bar{1}$0] orientation of the P level. Shown in Fig. 6 is the asymmetry in the potential profile due to *atomistic* strain and inequivalence in the piezoelectric potential along the [110] and [1$\bar{1}$0] directions at a certain height $z = 1$ nm from the base of the dots.

Figs. 7 and 8 show the conduction band wavefunctions for the ground and first three excited energy states in the dome-shaped and pyramidal QD structures with a diameter (base length) of 11.3 nm and height h of 5.65 nm, respectively. In Figs. 7(a) and 8(a), strain and piezoelectricity are *not* included in the calculation. The weak anisotropy in the P level is due to the atomistic interface and material discontinuity. Material discontinuity mildly favors the [110] direction in both the dots. In Figs. 7(b) and 8(b), atomistic strain and relaxation is included, resulting in 5.73-meV (dome) and 10.85-meV (pyramidal) splits in the P energy levels. Strain favors the [110] direction in both the dots. In Figs. 7(c) and 8(c), piezoelectricity is included at the top of strain, inducing a split of -2.84 meV (dome) and 9.59 meV
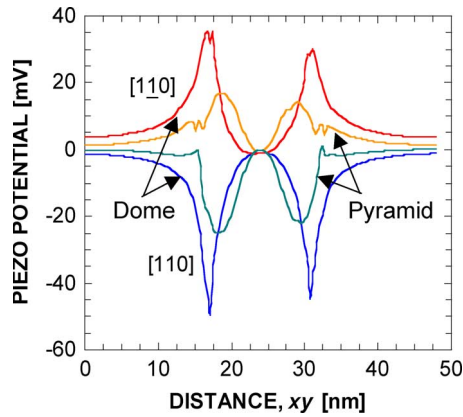
Fig. 6. Potential along the [110] and [1$\bar{1}$0] directions at $z = 1$ nm from the base of the dot. Notice the induced polarization in the potential profile and the unequal values of potential along the [110] and [1$\bar{1}$0] directions. In addition, the dome-shaped dot induces stronger potential ($d/b = 11.3$ nm and $h = 5.65$ nm).
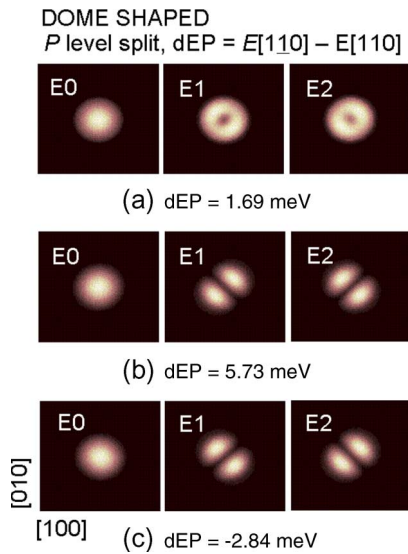

Fig. 7. Conduction band wavefunctions for the first three energy levels in the dome-shaped QD structure with base $b = 11.3$ nm and height $h = 5.65$ nm. (a) Without strain and piezoelectricity, $E_{[1\bar{1}0]} - E_{[110]} = 1.69$ meV. (b) With atomistic strain, $E_{[1\bar{1}0]} - E_{[110]} = 5.73$ meV. (c) With strain and piezoelectricity, $E_{[1\bar{1}0]} - E_{[110]} = -2.84$ meV. Piezoelectricity *flips* the wavefunctions.
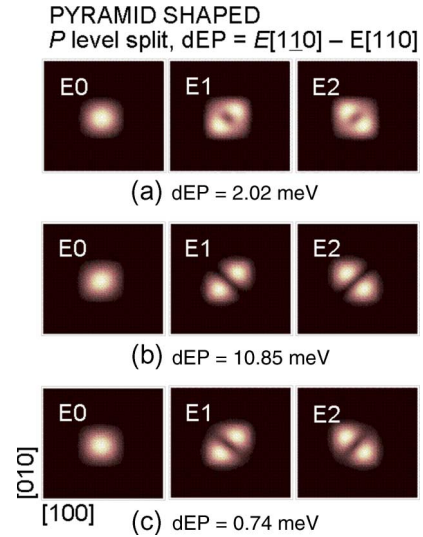

Fig. 8. Conduction band wavefunctions for the first three energy levels in the pyramidal QD structure with base $b = 11.3$ nm and height $h = 5.65$ nm. (a) Without strain and piezoelectricity, $E_{[1\bar{1}0]} - E_{[110]} = 2.02$ meV. (b) With atomistic strain, $E_{[1\bar{1}0]} - E_{[110]} = 10.85$ meV. (c) With strain and piezoelectricity, $E_{[1\bar{1}0]} - E_{[110]} = 0.74$ meV. Piezoelectricity does *not* flip the wavefunctions.
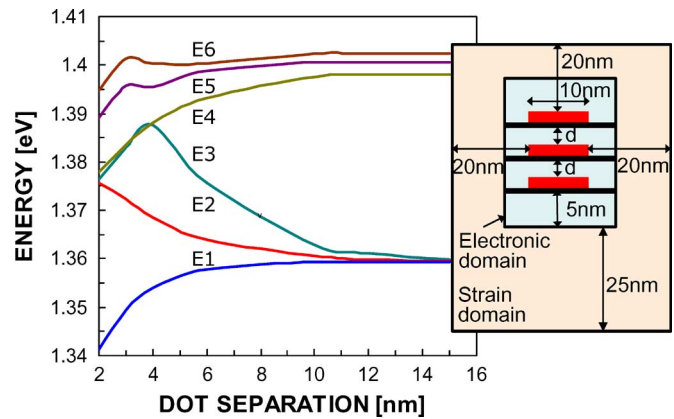

Fig. 9. Electron state energies in the QD molecule as a function of interdot separation. The strain simulation domain contains atoms ranging from 8 to 13 million, and the electronic structure domain contains atoms ranging from 0.5 to 1.1 million.

(pyramid) in the P energy level. There is a noticeable difference in Figs. 7(c) and 8(c). In the case of a dome-shaped dot [Fig. 7(c)], the first P state is oriented along the [1$\bar{1}$0] direction, and the second state is oriented along the [110] direction; piezoelectricity thereby has not only introduced a global shift in the energy spectrum but also *flipped* the orientation of the P states [20]. In the case of a pyramidal dot [Fig. 8(c)], the energetic sequence of the P states remains unchanged. The underlying reason behind this difference in orientation polarization due to piezoelectricity can be explained by the unequal potential induced, as depicted in the 1-D potential plot in Fig. 6, which really is induced by the off-diagonal crystal distortion that is depicted in Fig. 4. The pyramidal dot does not build up as much off-diagonal strain due to the alignment of its facets with the crystal. As a result, the piezoelectric fields are reduced.

B. Stacked QD System

SAQDs can be grown as stacks where the QD distance can be controlled with atomic layer control. This distance determines the interaction of the artificial atom states to form artificial molecules. The design of QD stacks becomes complicated since the structures are subject to inhomogeneous long-range strain and growth imperfections, such as nonidentical dots and interdiffused interfaces. QD stacks consisting of three QD layers are simulated next (see inset of Fig. 9). The InAs QDs are disk shaped with a diameter of 10 nm and a height of 1.5 nm that is positioned on a 0.6-nm-thick wetting layer. The substrate thickness under the first wetting layer is kept constant at 30 nm, and the cap layer on top of the topmost dot is kept at 10 nm for all simulations. The strain simulation domain contains atoms in the range of 8–13 million, and the electronic structure domain contains atoms in the range of 0.5–1.1 million.
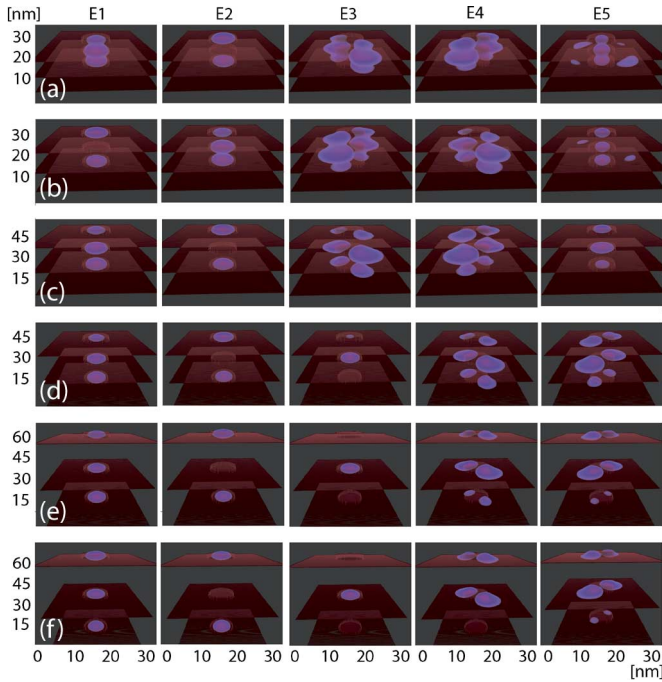
Fig. 10.　(Columns) First five electron states wavefunction magnitudes with (rows) 2-, 3-, 4-, 6-, 10-, and 12-nm QD separation.

Fig. 11.　(a) Schematic of a SiGe/Si/SiGe QW heterostructure grown on the [001] substrate. The crystal symmetry directions are along x and z. (b) Schematic of a QW unit cell grown on $z'[\bar{1}0n]$ miscut substrate. The unit cell is periodic along the $x'[n01]$-direction and y'-direction, and confined in the $z'[\bar{1}0n]$-direction. The miscut angle is $\theta_T = \tan^{-1}(1/n)$. The step height is one atomic layer $(a/4)$, where a is lattice constant. (c) Band structure of 5.26-nm-thick flat QW along x and $2°$ miscut QW along the x'-direction. Flat QW shows the presence of two nondegenerate valleys that are separated by an energy that is known as VS. Miscut QW shows the presence of two degenerate valleys that are centered at $\pm k_{x'}^0$. Interaction between these valleys at $\pm k_{x'} = 0$ causes a minigap (Δ_m), as shown in the inset. The lowest valleys are degenerate. Here, $a_L = na_{\text{Si}}$, and $n = 28$ for $2°$ miscut. SiGe buffer layers are not included in electronic structure calculation domain for these plots.

Fig. 9 shows the electron state energy as a function of interdot separation. In a system without inhomogeneous strain, one would expect the identical dots to have degenerate eigenstate energies for large dot separations. Strain breaks the degeneracy, even for large separations. The strain field clearly extends over the distance of 15-nm QD separation (which is why they physically do not grow on top of each other). As the dot separation is narrowed, the dots interact with each other mechanically through the strain field as well as quantum mechanically through wavefunction overlaps. The set of lowest states E1–3 clearly shows the state repulsion of bonding and antibonding molecular states for short interdot distances. Fig. 10 shows cross-sectional cuts in the growth direction and one lateral direction through the middle of the 3-D wavefunctions. The wavefunctions are quite clearly separated into the individual dots, with little overlap across the dots for dot separations of 12 and 10 nm. For separation in the range of 2–6 nm, wavefunction overlap can be observed. The reduction of E3 energy with decreasing distance in the range of 2–4 nm can be associated with a crossover of p-symmetry states. The electronic states and wavefunctions in a coupled QD system are thus determined through a complicated interplay of strain, QD size, and wavefunction overlap. Only a detailed simulation can reveal that interplay.

C. SiGe QW

Miscut (vicinal) surfaces [Fig. 11(b)], as opposed to flat surfaces [Fig. 11(a)], are often used to ensure uniform growth of Si/SiGe heterostructures. Miscut has a dramatic effect on the band structure of Si QW. The band structure of a flat Si QW has two valleys that are centered at $\pm k_x = 0$ and separated by an energy known as VS [24], [25]. VS in a flat QW is a result
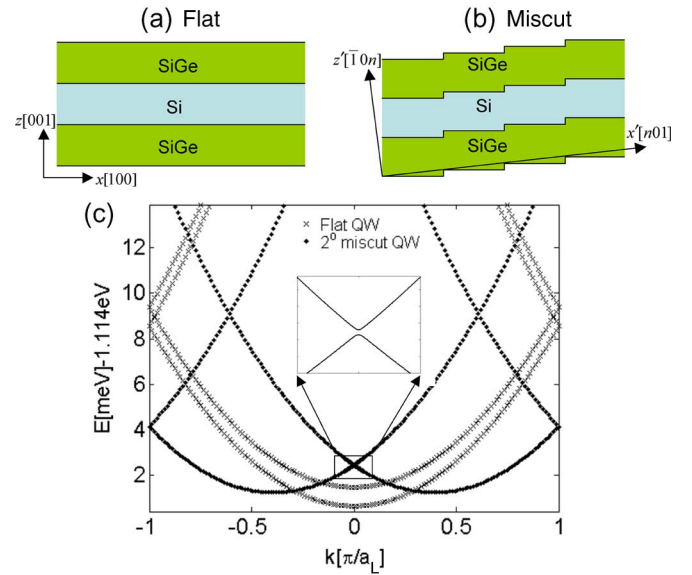
of interaction among states in bulk z-valleys that are centered at $k_z = k_m$, where k_m is the position of the valley-minimum in strained Si. In a miscut QW, the lowest lying valleys are degenerate with minima at $\pm k_{x'}^0$. Valley–valley interaction at $\pm k_x = 0$ causes the formation of a minigap Δ_m. Thus, atomic scale modulation of surface topology leads to very different electronic structures in flat and miscut QWs. As a consequence of this, flat and miscut QWs respond differently to the applied magnetic fields. In the presence of lateral confinement in miscut QW, the two degenerate valleys in Fig. 11(c) interact, giving rise to VS.

The VS can be measured using magnetic probe techniques, such as Shubnikov de Haas oscillations or electron-valley resonance [26], [27]. In these measurements, in-plane confinement of the Landau levels (LLs) is provided by the magnetic field. Fig. 12(a) and (b) shows the dependence of VS on the applied magnetic field in flat and $2°$ miscut QWs. In a flat QW, VS is independent of the magnetic field because in these QWs, VS arises from z-confinement that is provided by the confining SiGe buffers. In miscut QWs, however, VS arises from the interaction of two degenerate valleys that are centered at $\pm k_{x'}^0$ along the x'-direction. Therefore, x' confinement arising from the applied magnetic field results in the dependence of VS on the magnetic field. At low magnetic fields, this dependence is linear. The SiGe alloy disorder that is shown in the inset of Fig. 12(a) is inherently present in Si/SiGe heterostructures. In tight-binding calculations, alloy disorder translates into atom disorder and inhomogeneous strain disorder.
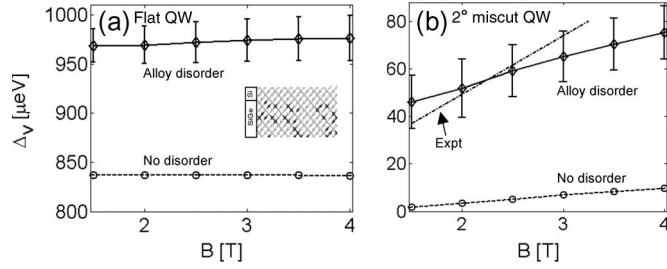
Fig. 12. (a) VS of the first LL in a 10-nm-thick flat strained Si QW. VS increases due to the alloy disorder (as shown in the inset) in SiGe buffer layers. (b) VS of the first LL in a $2°$ miscut strained Si QW. The presence of miscut surfaces leads to significant suppression in VS. Inclusion of realistic alloy disorder in SiGe buffer layers raise the VS to experimentally observed values. Error bars represent standard deviation in VS.

Strain disorder is known to have long-range nature (see, for example, the QD simulations in Fig. 2). SiGe layers measuring 40 nm are included at the top and the bottom of 10-nm Si QW for strain calculations. This SiGe thickness is sufficient to model the long-range strain disorder, where the detailed strain boundary conditions are not important and the SiGe volume exceeds the Si QW volume significantly. SiGe buffers provide electronic confinement of approximately 100 meV, because of which the electronic states of interest in this problem are spatially confined to the QW and only weakly penetrate into the SiGe buffer. Therefore, one can safely reduce the electronic structure domain to 3 nm of the SiGe buffer around the Si QW. For this setup, the strain calculation requires 3.6 million atoms, and the electronic structure calculation requires 0.7 million atoms. For the idealized geometries without a SiGe buffer, a homogeneous lattice distortion of $\varepsilon_{\parallel} = 0.013$ is assumed throughout the Si QW, as approximated from the full-SiGe buffer system calculation and hard wall boundary conditions are assumed in the z-direction. Such electronic structure calculations require $\sim 50\,000$ atoms.

The magnetic field is introduced into the tight-binding Hamiltonian through Peierls substation [28]–[30]. x' confinement resulting from the magnetic field is incorporated through the Landau gauge $(\vec{A} = Bx\hat{y})$. Closed boundary conditions are used in the x- and z-directions, while the y-direction is assumed to be (quasi-)periodic. The confinement that is induced by closed boundary conditions in the x'-direction competes with the magnetic field confinement. The lateral extension of the strain and the electronic structure domain is set to 150 nm, which is about seven times larger than the maximum magnetic confinement length in a 2-D electron gas (2DEG) at $B = 1.5$ T (21 nm). For the magnetic field range of 1.5–4 T, confinement is dominated by the magnetic field, and no lateral x-confinement effects due to the closed boundary conditions are visible in the simulations of Fig. 12. Modulation doping in Si/SiGe heterostructures induces a built-in electric field. In the simulations performed here, an electric field of 9 MV/m is assumed in the growth direction. The SiGe alloy disorder is assumed to be quasi-periodic in y-direction with the period of 5.5 nm, which is sufficient to capture the effect of inhomogeneous strain disorder.

In the presence of the applied magnetic field, the 2DEG is quantized in LLs. The valley degeneracy of LLs is broken in the presence of sharp confinement due to Si/SiGe interfaces in a QW. The VS of the first LL in flat and $2°$ miscut QWs is plotted as a function of the applied magnetic field in Fig. 12. The VS in ideal (no SiGe disorder) miscut QWs is two orders of magnitude less than that in flat QWs. The SiGe alloy disorder provides additional symmetry breaking, leading to enhancement in VS in flat as well as miscut QWs (Fig. 12). Addition of SiGe buffers to the electronic structure calculation domain in $2°$ miscut QWs results in VS close to the experimentally observed values.

Previous predictions of VS [24], [25] overpredict the value of the VS compared to experimental data [26], [27], while perfect slanted QWs underpredict the observed VS by an order of magnitude. Friesen *et al.* [31] suggest that the disorder in the miscuts raises the VS to experimentally observed levels. Here, we show that buffer disorder with regular miscut steps alone can account for the additional VS. We do not have to assume any particular step disorder models at all [32]. The atomistic representation of the confinement buffer and the local disorder in it is therefore an essential ingredient in the physics-based simulation of VS. No additional disorder parameters need to be introduced to obtain results that are close to those obtained in the experiments! Simulations including step roughness disorder combined with alloy disorder have recently been shown [32] to improve the agreement with experiment.

D. SiGe Nanowires

Nanowires conduct carriers in one dimension and confine them in the other two dimensions. As the wire diameter is reduced to the nanometer range, it is understood that the 2-D confinement modifies the electronic structure and that the nanowire is quite similar to an electromagnetic waveguide. Typical calculations are performed in the single band effective mass calculation. Full 3-D transport simulations based on the nonequilibrium Green's function (NEGF) have been implemented in simulators [13], analyzed for interface roughness [33], and released on the nanoHUB [34]. Since its release in May 2006, the nanowire code has been used by more than 612 users who have run more than 8970 simulations on a parallel virtual cluster utilizing VIOLIN [35], indicating that there is a real demand in the community for such simulations. It is however also understood that, as the nanowire dimension shrinks to below 5 nm, the effective mass approximation breaks down [36], and an atomistic representation of the material is needed to compute the dispersion of an ideal nanowire slice. Efforts are now underway to develop full 3-D nanowire NEGF-based transport simulators that are fully atomistic [15]. Fundamental questions to be addressed here remain the influence of the nanowire interface and the atomistic nanowire composition, such as alloy disorder.

Recently, NEGF-based transport simulations and full 3-D electronic structure calculations were compared for AlGaAs nanowires [16]. A critical finding of that work was that the alloy disorder strongly influences the dispersion along the wire direction. The considered AlGaAs wires are unstrained and "only" contain atom disorder, while all atom positions are on a regular zincblende GaAs/AlAs lattice. This paper presents for the first time electronic structure calculations for SiGe nanowires that
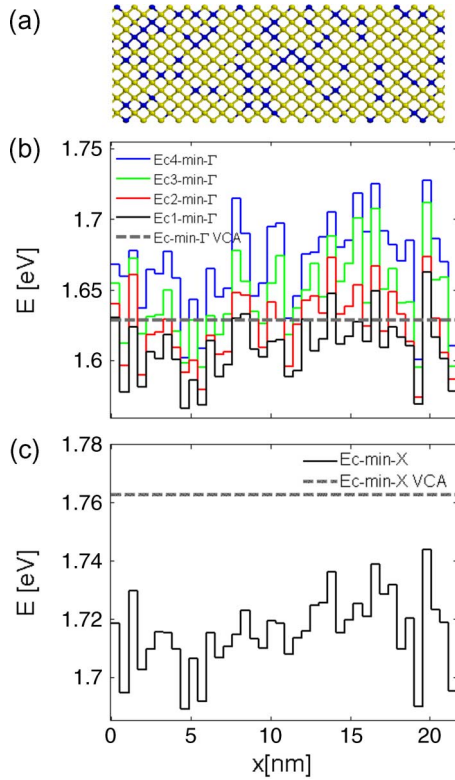
Fig. 13. (a) Atomistically resolved disorder in the $Si_{0.8}Ge_{0.2}$ $40 \times 4 \times 4$ nanowire. (b) Band-edge minima of the first four conduction subbands plotted along the length of the nanowire in local band structure and VCA formulations. (c) Band-edge minimum in the transport direction plotted along the length of the nanowire.

contain strain, position, and atom disorder. Different nanowire cross sections with four, six, and eight unit cells, corresponding to 2.17, 3.26, and 4.34 nm with a common nanowire length of 40 unit cells, corresponding to 22 nm, are considered. Strain and electronic structure calculations are performed on the whole nanowire in free-standing configuration. In other words, the substrate is not taken into account.

Fig. 13(a) depicts a sliver cut through the center of the $40 \times 4 \times 4$ sample, indicating the atomistically resolved disorder of the wire. Only the central 5-nm-long portion of this 22-nm-long wire is shown for good atomistic resolution. It is obvious that there is no such thing as a repeated unit cell in that wire. Therefore, the very concept of band structure, which is based on a (small) repeated cell in semiconductors is called into question [37]. The most typical approach to deal with alloy disorder is called virtual crystal approximation (VCA). The VCA averages the atomic potentials according to the atom concentrations to smooth out the material. In that approach, a band structure can be easily calculated in the repeated 4×4 unit cell.

In another approach, one can consider a single sliver of the 4×4 building block, imagine that this cell is repeated infinitely, and compute a band structure in it. This would, in a sense, represent the local band structure for each slice. With the fluctuations in the device, one would expect that the conduction band edge will fluctuate from slice to slice, as indicated in Fig. 13(b). The SiGe alloy disorder splits four fourfold degenerate bands in a pure Si nanowire. The corresponding band-edge minima of
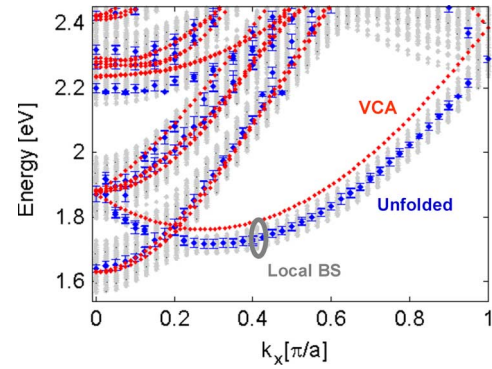

Fig. 14. Band structures of the $40 \times 4 \times 4$ $Si_{0.8}Ge_{0.2}$ alloy nanowire in (gray) local band structure, (red) VCA, and (blue) zone-unfolding formulations.

these four bands in $40 \times 4 \times 4$ SiGe alloy nanowire are plotted along the length of the nanowire in Fig. 13(b). The four bands are degenerate in the VCA formulation, and the band-edge minimum of this band is also plotted in Fig. 13(b). Fig. 13(c) shows the X-point conduction band minimum along the wire length in local band structure and VCA formulation. Each slice has its own local band structure, and its fluctuations in k-space are compared in Fig. 14 against the VCA approach. This local band structure approach does not deliver a meaningful band edge of the wire or a meaningful effective mass.

An alternative approach to the local band structure and the VCA approach is the computation of the electronic structure of the overall wire to extract an approximate band structure that describes the overall wire well [37]. This approximate band structure is representative of the overall transport capabilities of the wire and correlates well to NEGF transport simulations [16]. Fig. 14 also compares the approximate band structure to the VCA and the local band structure samples. The approximate band structure provides a much more meaningful representation of the nanowire performance than the other two, which either overrepresent the disorder or ignore disorder completely. From this approximate dispersions, one can derive critical device parameters such as band gap and effective masses (along the transport direction), which can be used in an approximate over-the-barrier-model to predict device performance [17], [38].

Band gaps and effective masses are plotted as a function of nanowire diameter in Fig. 15(a) and (b). The approximate band structure predicts a smaller band gap than the VCA similar to AlGaAs nanowires [16] and AlGaAs bulk [39]. The direct (Δ_4) and indirect (Δ_2) valley band gaps show an interesting crossover for 4.34-nm wires, which will significantly increase the density of states at the conduction band edge and influence device performance; the VCA assumption does not result in such a crossover. Interestingly, the VCA and approximate band structure result in virtually identical effective masses. Additional statistical samples on different wires need to be simulated in the future to verify if this is a typical trend for this class of SiGe wires.

Since the band structure is approximate, it does contain an error bar in energy for each k point in the dispersion. These energy uncertainties can be used to calculate the scattering time of the state according to the prescription of [40]. One would expect that, as the system becomes larger, the error bars become
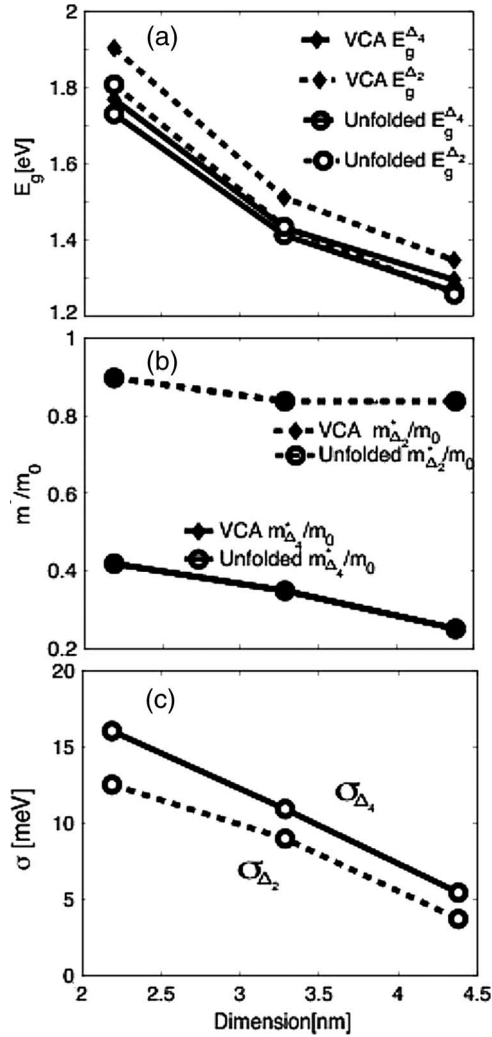
Fig. 15. (a) Direct (Δ_4 valleys) and indirect (Δ_2 valleys) band gaps obtained from VCA and zone-unfolded band structures. (b) Effective masses of Δ_4 and Δ_2 valleys. (c) Energy uncertainties of Δ_4 and Δ_2 bands. The effective masses for each valley are almost the same in the VCA and unfolded cases so that the curves coincide.

smaller and the system becomes more bulklike. Fig. 15(c) depicts the size of the error bars at the Δ_4 and Δ_2 valley conduction band edges and indeed confirms that expectation. Note that, even for the 4.34-nm-thick nanowire, the fluctuations are still on the order of 5 meV.

III. CONCLUSION

NEMO 3-D is introduced to the IEEE Nanoelectronics community as a versatile open-source electronic structure code that can handle device domains that are relevant for realistic devices. Realistic devices containing millions of atoms can be computed with reasonably easily available cluster computers. NEMO 3-D employs a valence-force field Keating model for strain and the 20-band $sp^3d^5s^*$ empirical tight-binding model for the electronic structure computation. The impact of atomistic strain and piezoelectricity on the electronic structure in dome-shaped QDs is explored. Under the assumptions of realistic boundary conditions, strain is found to be long ranged and to penetrate about 20 nm into the dot substrate, thus stressing the

need for using large dimensions of these surrounding layers and at least three million atoms in the simulations. The true symmetry of the QDs is found to be lower than the geometrical shape symmetry because of the fundamental atomistic nature of the underlying zincblende crystal lattice. Atomistic strain is found to induce further optical polarization anisotropy favoring the [110] direction and pronounced nondegeneracy in the QD excited states, the magnitude (few millielectronvolt) of which depends mainly on the dot size and surrounding material matrix. First-order piezoelectric potential, on the other hand, favors the [1$\underline{1}$0] direction, reduces the nondegeneracy in the P states, and is found to be strong enough to *flip* the optical polarization in certain sized QDs [20]. Simulations of QD stacks exemplify the complicated mechanical strain and quantum mechanical interactions on confined electronic states. Molecular states can be observed when the dots are in close proximity. Simulations of SiGe-buffered Si QWs indicate the importance of band-to-band interactions that are naturally understood in the NEMO 3-D basis. VS is computed as a function of the magnetic field matching experimental data. The first simulations of disordered SiGe alloyed nanowires indicate the critical importance of the treatment of atomistic disorder. Typical approaches of a smoothed-out material (VCA) or considerations of band structure in just individual slices clearly fail to represent the disordered nanowire physics.

NEMO 3-D demonstrates the capability to model a large variety of relevant realistically sized nanoelectronic devices. It is released under an open-source license and maintained by the NCN—an organization dedicated to develop and deploy advanced nanoelectronic modeling and simulation tools. NEMO 3-D is not limited to research computing alone; The first educational version including visualization capabilities has been released on https://www.nanohub.org. and has been used by hundreds of users for thousands of simulations.

REFERENCES

[1] P. M. Petroff, *Single Quantum Dots: Fundamentals, Applications, and New Concepts*, P. Michler, Ed. Berlin, Germany: Springer-Verlag, 2003.
[2] P. Michler, A. Kiraz, C. Becher, W. V. Schoenfeld, P. M. Petroff, L. Zhang, E. Hu, and A. Imamolu, "A quantum dot single-photon turnstile device," *Science*, vol. 290, no. 5500, pp. 2282–2285, Dec. 2000.
[3] E. Moreau, I. Robert, L. Manin, V. Thierry-Mieg, J. Gérard, and I. Abram, "Quantum cascade of photons in semiconductor quantum dots," *Phys. Rev. Lett.*, vol. 87, no. 18, p. 183 601, Oct. 2001.
[4] M. A. Reed, J. N. Randall, R. J. Aggarwal, R. J. Matyi, T. M. Moore, and A. E. Wetsel, "Observation of discrete electronic states in a zero-dimensional semiconductor nanostructure," *Phys. Rev. Lett.*, vol. 60, no. 6, pp. 535–537, Feb. 1988.

[5] M. A. Reed, "Quantum dots," *Sci. Amer.*, vol. 268, no. 1, pp. 118–123, 1993.

[6] Y. Arakawa and H. Sasaki, "Multidimensional quantum well laser and temperature dependence of its threshold current," *Appl. Phys. Lett.*, vol. 40, no. 11, pp. 939–941, Jun. 1982.

[7] S. Fafard, K. Hinzer, S. Raymond, M. Dion, J. Mccaffrey, Y. Feng, and S. Charbonneau, "Red-emitting semiconductor quantum dot lasers," *Science*, vol. 274, no. 5291, pp. 1350–1353, Nov. 1996.

[8] M. V. Maximov, Y. M. Shernyakov, A. F. Tsatsul'nikov, A. V. Lunev, A. V. Sakharov, V. M. Ustinov, A. Y. Egorov, A. E. Zhukov, A. R. Kovsch, P. S. Kop'ev, L. V. Asryan, Z. I. Alferov, N. N. Ledentsov, D. Bimberg, A. O. Kosogov, and P. Werner, "High-power continuous-wave operation of a InGaAs/AlGaAs quantum dot laser," *J. Appl. Phys.*, vol. 83, no. 10, pp. 5561–5563, May 1998.

[9] B. E. Kane, "A silicon-based nuclear spin quantum computer," *Nature*, vol. 393, no. 6681, p. 133, May 1998.

[10] P. Chen, C. Piermarocchi, and L. J. Sham, "Control of exciton dynamics in nanodots for quantum operations," *Phys. Rev. Lett.*, vol. 87, no. 6, p. 067 401, Aug. 2001.

[11] M. Usman, S. Ahmed, M. Korkusinski, C. Heitzinger, and G. Klimeck, "Strain and electronic structure interactions in realistically scaled quantum dot stacks," in *Proc. 28th ICPS*, Vienna, Austria, Jul. 24–28, 2006, p. 847.

[12] G. Klimeck, T. Boykin, M. Luisier, N. Kharche, and A. Schenk, "A study of alloyed nanowires from two perspectives: Approximate dispersion diagrams and transmission coefficients," in *Proc. 28th ICPS*, Vienna, Austria, Jul. 24–28, 2006, pp. 711–712.

[13] J. Wang, A. Rahman, A. Ghosh, G. Klimeck, and M. Lundstrom, "Performance evaluation of ballistic silicon nanowire transistors with atomic-basis dispersion relations," *Appl. Phys. Lett.*, vol. 86, no. 9, p. 093 113, Feb. 2005.

[14] Y. Zheng, C. Rivas, R. Lake, K. Alam, T. B. Boykin, and G. Klimeck, "Electronic properties of silicon nanowires," *IEEE Trans. Electron Devices*, vol. 52, no. 6, pp. 1097–1103, Jun. 2005. and references therein.

[15] M. Luisier, A. Schenk, W. Fichtner, and G. Klimeck, "Atomistic simulation of nanowires in the $sp^3d^5s^*$ tight-binding formalism: From boundary conditions to strain calculations," *Phys. Rev. B, Condens. Matter*, vol. 74, no. 20, p. 205 323, Nov. 2006.

[16] T. B. Boykin, M. Luisier, A. Schenk, N. Kharche, and G. Klimeck, "The electronic structure and transmission characteristics of disordered AlGaAs nanowires," *IEEE Trans. Nanotechnol.*, vol. 6, no. 1, pp. 43–47, Jan. 2007.

[17] A. Rahman, G. Klimeck, and M. Lundstrom, "Novel channel materials for ballistic nanoscale MOSFETs bandstructure effects," in *IEDM Tech. Dig.*, Washington, DC, Dec. 5–7, 2005, pp. 601–604.

[18] M. Prada, N. Kharche, and G. Klimeck, "Electronic structure of Si/InAs composite channels," in *Proc. Symp. G: Extending Moore's Law With Adv. Channel Mater*. Accepted as oral presentation in MRS Spring conference 2007.

[19] M. A. Eriksson, M. Friesen, S. N. Coppersmith, R. Joynt, L. J. Klein, K. Slinker, C. Tahan, P. M. Mooney, J. O. Chu, and S. J. Koester, "Spin-based quantum dot quantum computing in Silicon," *Quantum Inf. Process.*, vol. 3, no. 1–5, pp. 133–146, 2004.

[20] G. Bester and A. Zunger, "Cylindrically shaped zinc-blende semiconductor quantum dots do not have cylindrical symmetry: Atomistic symmetry, atomic relaxation, and piezoelectric effects," *Phys. Rev. B, Condens. Matter*, vol. 71, no. 4, p. 045 318, Jan. 2005. Also, please see references therein.

[21] S. Lee, O. L. Lazarenkova, F. Oyafuso, P. von Allmen, and G. Klimeck, "Effect of wetting layers on the strain and electronic structure of InAs self-assembled quantum dots," *Phys. Rev. B, Condens. Matter*, vol. 70, no. 12, p. 125 307, Sep. 2004.

[22] S. Lee, F. Oyafuso, P. von Allmen, and G. Klimeck, "Boundary conditions for the electronic structure of finite-extent, embedded semiconductor nanostructures with empirical tight-binding model," *Phys. Rev. B, Condens. Matter*, vol. 69, no. 4, p. 045 316, Jan. 2004.

[23] G. Bester, X. Wu, D. Vanderbilt, and A. Zunger, "Importance of second-order piezoelectric effects in Zinc-Blende semiconductors," *Phys. Rev. Lett.*, vol. 96, no. 18, p. 187 602, May 2006.

[24] T. B. Boykin, G. Klimeck, M. Eriksson, M. Friesen, S. N. Coppersmith, P. von Allmen, F. Oyafuso, and S. Lee, "Valley splitting in strained silicon quantum wells," *Appl. Phys. Lett.*, vol. 84, no. 1, pp. 115–117, Jan. 2004.

[25] T. B. Boykin, G. Klimeck, M. A. Eriksson, M. Friesen, S. N. Coppersmith, P. von Allmen, F. Oyafuso, and S. Lee, "Valley splitting in low-density quantum-confined heterostructures studied using tight-binding models," *Phys. Rev. B, Condens. Matter*, vol. 70, no. 16, p. 165 325, Oct. 2004.

[26] S. Goswami, M. Friesen, J. L. Truitt, C. Tahan, L. J. Klein, J. O. Chu, P. M. Mooney, D. van der Weide, S. N. Coppersmith, R. Joynt and M. A. Erikson, cond-mat/0408389.

[27] S. Goswami, K. A. Slinker, M. Friesen, L. M. McGuire, J. L. Truitt, C. Tahan, L. J. Klein, J. O. Chu, P. M. Mooney, D. W. van der Weide, R. Joynt, S. N. Coppersmith and M. A. Eriksson, cond-mat/0611221.

[28] T. B. Boykin and P. Vogl, "Dielectric response of molecules in empirical tight-binding theory," *Phys. Rev. B, Condens. Matter*, vol. 65, no. 3, p. 035 202, Jan. 2001.

[29] M. Graf and P. Vogl, "Electromagnetic fields and dielectric response in empirical tight-binding theory," *Phys. Rev. B, Condens. Matter*, vol. 51, no. 8, pp. 4940–4949, Feb. 1995.

[30] T. B. Boykin, R. Chris Bowen, and G. Klimeck, "Electromagnetic coupling and gauge invariance in the empirical tight-binding method," *Phys. Rev. B, Condens. Matter*, vol. 63, no. 24, p. 245 314, Jun. 2001.

[31] M. Friesen, M. A. Eriksson, and S. N. Coppersmith, "Magnetic field dependence of valley splitting in realistic Si/SiGe quantum wells," *Appl. Phys. Lett.*, vol. 89, no. 20, p. 202 106, Nov. 2006.

[32] N. Kharche, M. Prada, T. B. Boykin, and G. Klimeck, "Valley-splitting in strained Silicon quantum wells modeled with 2 degree miscuts, step disorder, and alloy disorder," *Appl. Phys. Lett.*, vol. 90, no. 9, p. 092 109, Sep. 2007.

[33] J. Wang, E. Polizzi, A. Ghosh, S. Datta, and M. Lundstrom, "Theoretical investigation of surface roughness scattering in silicon nanowire transistors," *Appl. Phys. Lett.*, vol. 87, no. 4, p. 043 101, Jul. 2005.

[34] [Online]. Available: https://www.nanohub.org/simulation_tools/nanowire_tool_information

[35] P. Ruth, J. Rhee, D. Xu, R. Kennell, and S. Goasguen, "Autonomic live adaptation of virtual computational environments in a multi-domain infrastructure," in *Proc. IEEE ICAC*, 2006, pp. 5–14.

[36] J. Wang, A. Rahman, G. Klimeck, and M. Lundstrom, "Bandstructure and orientation effects in Si and Ge nanowire FETs," in *IEDM Tech. Dig.*, Washington, DC, Dec. 5–7, 2005, pp. 530–533.

[37] T. B. Boykin, N. Kharche, G. Klimeck, and M. Korkusinski, "Approximate bandstructures of semiconductor alloys from tight-binding supercell calculations," *J. Phys.: Condens. Matter*, vol. 19, no. 3, p. 036 203, Jan. 2007.

[38] J. Wang, E. Polizzi, and M. Lundstrom, "A three-dimensional quantum simulation of silicon nanowire transistors with the effective-mass approximation," *J. Appl. Phys.*, vol. 96, no. 4, pp. 2192–2203, Aug. 2004.

[39] F. Oyafuso, G. Klimeck, R. Chris Bowen, and T. B. Boykin, "Atomistic electronic structure calculations of unstrained alloyed systems consisting of a million atoms," *J. Comput. Electron.*, vol. 1, no. 3, pp. 317–321, Oct. 2002.

[40] T. B. Boykin, N. Kharche, and G. Klimeck, "Evolution time and energy uncertainty," *Eur. J. Phys.*, vol. 28, no. 4, pp. 673–673, Jul. 2007.

Gerhard Klimeck (S'93–M'94–SM'04) received the Dipl.Ing. degree in electrical engineering from Ruhr-University, Bochum, Germany, in 1990 and the Ph.D. degree from Purdue University, West Lafayette, IN, in 1994.

He was the Technical Group Supervisor for the Applied Cluster Computing Technologies Group and continues to hold his appointment as a Principal Member with the National Aeronautics and Space Administration Jet Propulsion Laboratory, California Institute of Technology, Pasadena, CA, on a faculty part-time basis. Previously, he was a member of Technical Staff with the Central Research Laboratory, Texas Instruments Incorporated. He has been the lead on the development of NEMO 3-D, a tool that enables the simulation of tens-of-million atom quantum dot systems, and NEMO 1-D, the first nanoelectronic CAD tool. He is currently the Technical Director of the Network for Computational Nanotechnology and a Professor of electrical and computer engineering with the School of Electrical and Computer Engineering, Purdue University. He leads the development and deployment of Web-based simulation tools that are hosted on http://nanohub.org, a community website that is utilized by over 22 000 users annually. His work is documented in over 170 peer-reviewed publications and over 270 conference presentations. His research interests include the modeling of nanoelectronic devices, parallel cluster computing, and genetic algorithms.

Dr. Klimeck is a member of American Physical Society, Eta Kappa Nu, and Tau Beta Pi.

Shaikh Shahid Ahmed received the B.S. degree in electrical and electronic engineering from the Bangladesh University of Engineering and Technology, Dhaka, Bangladesh, in 1998 and the M.S. and Ph.D. degrees in electrical engineering from Arizona State University, Tempe, AZ, in 2003 and 2005, respectively.

He is a Postdoctoral Research Associate with the School of Electrical and Computer Engineering and Network for Computational Nanotechnology, Purdue University, West Lafayette, IN. He has published more than 40 journal and conference proceeding articles and two book chapters in these and related fields. His research focuses mainly in the areas of atomistic electronic structure and quantum transport models and methodologies for nanostructures, including quantum dots and qubits, carbon nanotube and ribbons, nanowires and sensors, solid-state light; classical and nonclassical semiconductor device and process simulations; novel numerical algorithms, particularly for molecular dynamics and Green's function computation; large-scale high-performance parallel cluster and distributed computing and developing community nanotechnology application packages; and analog and digital design.

Neerav Kharche received the B.Tech. and M.Tech. degrees in metallurgical engineering and materials science from the Indian Institute of Technology, Bombay, India, in 2003. He is currently working toward the Ph.D. degree in electrical and computer engineering in the School of Electrical and Computer Engineering and Network for Computational Nanotechnology, Purdue University, West Lafayette, IN.

His research interests are in the area of electronic structure and quantum transport in nanoscale devices. He is currently working on modeling the effects of disorder on the electronic structure of nanowires and quantum wells.

Marek Korkusinski received the undergraduate degree from the Wroclaw University of Technology, Wroclaw, Poland, in 1998 and the Ph.D. degree from the University of Ottawa, Ottawa, ON, Canada, in 2004.

He is a Research Associate with the Quantum Theory Group, Institute for Microstructural Sciences, National Research Council of Canada, Ottawa. Prior to his current appointment, he collaborated with Prof. Gerhard Klimeck at Purdue University, West Lafayette, IN, on multimillion-atom computational projects. His research interests are in the area of theoretical condensed matter physics and include optical and electronic properties of semiconductor nanostructures, correlations in electronic and electron-hole systems, and nanospintronics. His current projects involve using the tb-DFT and ab initio methods in calculations of the properties of semiconductor and carbon-based nanostructures.

Muhammad Usman received the B.Sc. and M.Sc. degrees (with honors and distinctions) in electrical engineering from the University of Engineering and Technology, Lahore, Pakistan, in 2002 and 2004, respectively. He is currently working toward the Ph.D. degree in the School of Electrical and Computer Engineering and Network for Computational Nanotechnology, Purdue University, West Lafayette, IN.

His research is focused on electronic and strain calculations in coupled quantum dots and their optical applications.

Mr. Usman is a USA Fulbright Fellow.

Marta Prada received the Physics degree from the Universidad Autonoma de Madrid, Madrid, Spain, in 1998 and the Ph.D. degree from the University of Leeds, Leeds, U.K., in December 2005.

She was with the European Organization for Nuclear Research (CERN) for a couple of years. In 2006, she was with the School of Electrical and Computer Engineering and Network for Computational Nanotechnology, Purdue University, West Lafayette, IN, as a Postdoctoral Researcher.

Timothy B. Boykin (S'86–M'91–SM'05) received the B.S. degree (summa cum laude) in electrical engineering from Rice University, Houston, TX, in 1987 and the M.S. and Ph.D. degrees in electrical engineering from Stanford University, Stanford, CA, in 1988 and 1992, respectively.

He joined the Department of Electrical and Computer Engineering, University of Alabama in Huntsville (UAH) in September 1992, was promoted to Associate Professor in August 1997, and was awarded tenure in August 1998. He has been promoted to Full Professor effective August 2007. He is the author or coauthor of over 55 refereed journal articles, and his first authored papers alone have been cited by other (noncoauthor) researchers over 330 times. His research centers on detailed semiconductor heterostructure and device modeling. The highlights of his research include the first numerically stable localized-orbital basis heterostructure model, the impact of nonzero in-plane wavevector on tunneling, incompleteness in tight-binding models, improved methods for calculating boundary conditions in tight-binding models, optimizations and capabilities of tight-binding models, consequences of incompleteness for the quantum-mechanical continuity equation, the representation of electromagnetic effects in tight-binding models, valley splitting in silicon quantum wells, and modeling alloy nanostructures.

Dr. Boykin is a member of Phi Beta Kappa, Tau Beta Pi, Eta Kappa Nu, the American Physical Society, and Sigma Xi. He received the UAH Foundation Award for Research and Creative Achievement in Applied Science/Technology in 2001.